Supplementary Information (SI) for Inorganic Chemistry Frontiers.

Supporting Information

Stoichiometric composition	Notation
$Mg_3Y_2Ge_3O_{12}$	MYGO
$Mg_3Y_{1.994}Ge_3O_{12}$:0.006Eu^{3+}	MYGO:Eu
$Mg_3Y_{1.994}Ge_3O_{12}$:0.006Ce^{3+}	MYGO:Ce
$Mg_3Y_{1.994}Ge_3O_{12}$:0.006Pr^{3+}	MYGO:Pr
$Mg_3Y_{1.994}Ge_3O_{12}$:0.006Tb^{3+}	MYGO:Tb
$Mg_3Y_{1.988}Ge_3O_{12}$:0.006Pr^{3+},0.006Tb^{3+}	MYGO:Pr,Tb
$Mg_3Y_{2(1-x)}Ge_3O_{12}$:xPr^{3+} (0.1% ≤ x ≤ 0.6%)	MYGO:xPr
$Mg_3Y_{2(1-y)}Ge_3O_{12}$:yTb^{3+} (0.1% ≤ y ≤ 3.5%)	MYGO:yTb
$Mg_3Y_{2(0.997-y)}Ge_3O_{12}$:0.006$Pr^{3+}$,y$Tb^{3+}$ (0.1% ≤ y ≤ 3.5%)	MYGO:Pr,yTb

Table S1 Stoichiometric compositions and notations of the samples.

Formula	$Mg_3Y_2Ge_3O_{12}$
Crystal system	cubic
Space group	*Ia3d(230)*
Lattice parameters	
a (Å)	*a = 12.2489 Å*
b (Å)	*b = 12.2489 Å*
c (Å)	*c = 12.2489 Å*
Reliability factor	
Rwp	13.29%
Rp	8.31%
χ^2	2.26

Table S2 XRD refined parameters of the MYGO host.

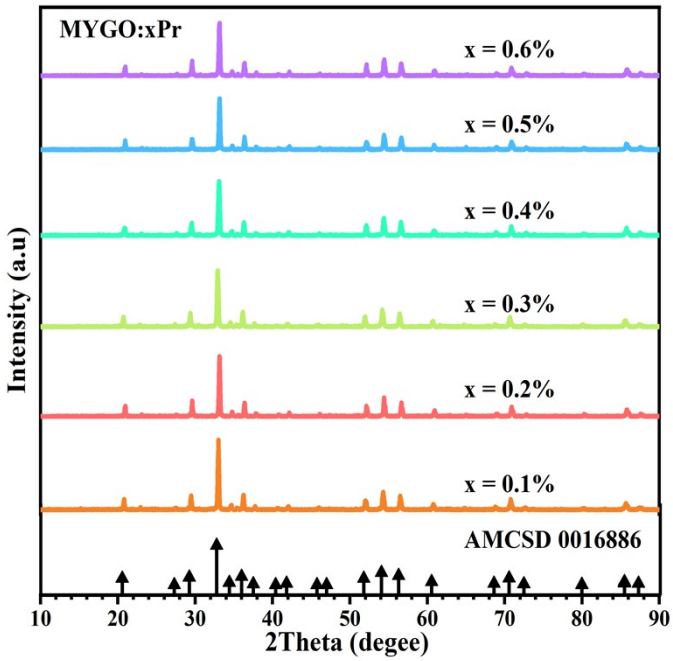

Fig. S1 X ray diffraction patterns of the as-synthesized MYGO:xPr at the concentration range of 0.1% ≤ x ≤ 0.6%.

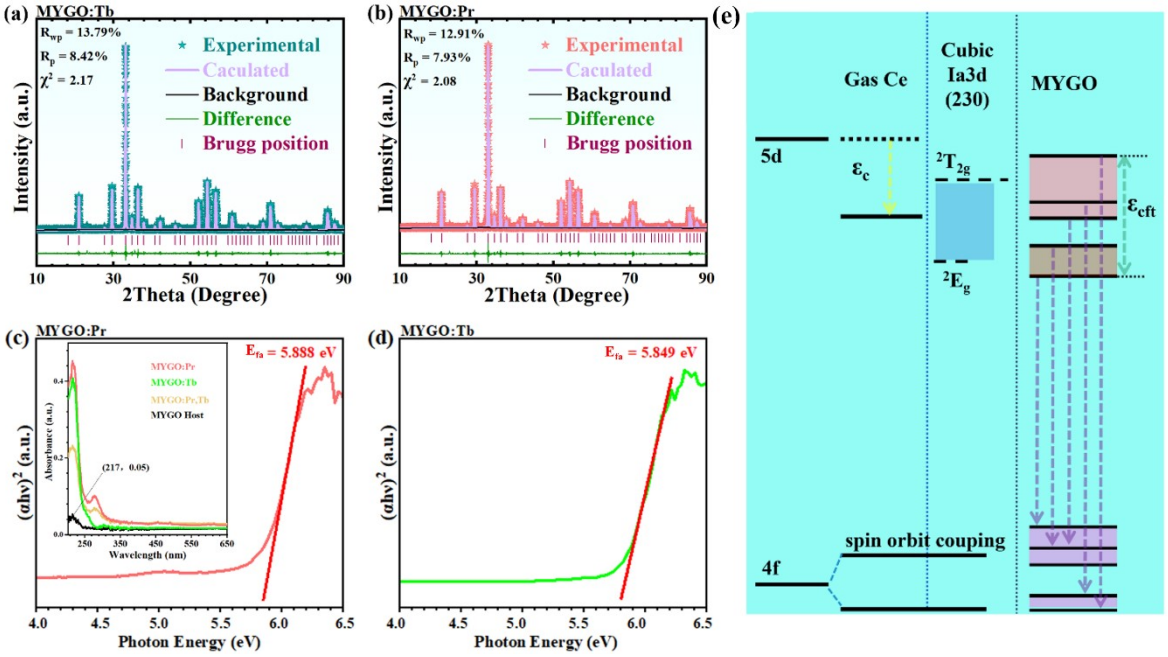

Fig. S2 (a-b) Rietveld refinement performed on the XRD of MYGO:Pr (a) and MYGO:Tb (b). (c-d) the DRS of MYGO:Pr (c) and MYGO:Tb (d). (e) Schematic Energy level structure of a free gas Ce^{3+}, Ce^{3+} ion at Y^{3+} position in MYGO:Ce.

To shed light on the ion-dependent luminescence mechanism, the UVV-DRS of the undoped MYGO host was analyzed, as located in **Fig. 1(e-f)** and **Fig. S2(c-d)** in the RT, what shows that the undoped MYGO host has an absorption of 210-270 nm. The optical band gap of the host can be roughly estimated by formula S(1):[1, 2]

$$[F(R_\infty)h\nu]^{1/n} = A(h\nu - E_{fa}) \quad (1)$$

where $F(R_\infty)$, $h\nu$ and A represent the Kubelka Munk absorption coefficient function, energy per photon, and proportionality constant, respectively. The transition coefficient n = 1/2, 2 denotes the direct allowed and indirect allowed, respectively, and the E_{fa} is the fundamental absorption threshold of MYGO.[3] The absorption coefficient

function of $F(R_\infty)$ could be written as the formula S(2):[1]

$$F(R_\infty) = (1 - R)^2/2R = K/S \quad (2)$$

in which *S*, *K*, and *R* represent the scattering parameter, absorption, and reflection coefficient, respectively. The absorption spectrum of MYGO was calculated using the Kubelka Munk equation is depicted in Fig. 1e. From the extrapolation of the line for $[F(R_\infty)hv]^2 = 0$, the E_{fa} values were calculated to 5.626 (host) 5.888 (Pr), 5.849 (Tb) and 5.855 (Pr and Tb) eV respectively. It is clear that the absorption edge blue-shifted with the Ln^{3+} doping in MYGO. The most possible reason is as follows:

When Ln^{3+} is introduced into the MYGO lattice to replace Y^{3+}, the crystal field strength (D_q) around Ln^{3+} can be estimated with the following Equation (3):[3,4]

$$D_q = Ze^2r^4/6R^5 \quad (3)$$

where D_q is the energy level separation, Z is the anion valence, e is the electron charge, *r* is the radius of the d wave function, and *R* is the distance between the central ion and its ligands. According to formula (3), D_q is inversely proportional to the fifth power of the average bond length (R_{ave}). The crystal field strength (proportional to the D_q) around Ln^{3+} in MYGO:Ln became smaller, due to the larger radius of Ln^{3+} compared to that of Y^{3+} (R_{ave} is proportional to the radius). A smaller D_q will cause a blue shift in the PL spectra. It is reasonable to assume that the PLE spectra are correspondingly blue-shifted with the PL spectra. In general, the trend of the UVV DRS is similar to that of the PLE spectrum. Therefore, the absorption edge of MYGO:Ln has blue-shifted.

The energy position of the $4f^7$-$4f^65d^1$ translation of Ce^{3+} in the host is influenced by two aspects: the crystal field splitting (ε_{cfs}) and the nephelauxetic effect (ε_c).[5] The 5d energy level of Ce^{3+} splits into two sets of excited states ($^2T_{2g}$ and ^2E_g) when it occupies a site with ideal D2d symmetry.[3] When the ideal D2d symmetry is distorted, the $^2T_{2g}$ and ^2E_g states will further split into five sub-levels.[6] In MYGO:Ce, the introduction of Ce^{3+} (103.4 Å, CN = 8) leads to the decrease in Rave and consequently to an increase in D_q, while ε_{cfs} is positively correlated with D_q, thus leading to lattice distortion and a larger crystal field splitting that divides the $^2T_{2g}$ and ^2E_g states into five sub-levels.[4] It is well known that the emission of a Ce^{3+} is generated by the translation from the lowest 5d excited state to the $^2F_{5/2}$ and $^2F_{7/2}$ ground states,[3] so the PLE spectrum can be decomposed by the Gaussian fit into five excitation bands located at 300.0, 319.0, 335.8, 426.6 and 458.4 nm (4.13, 3.89, 3.69, 2.91 and 2.71 eV), respectively, as shown in Fig. S2e.

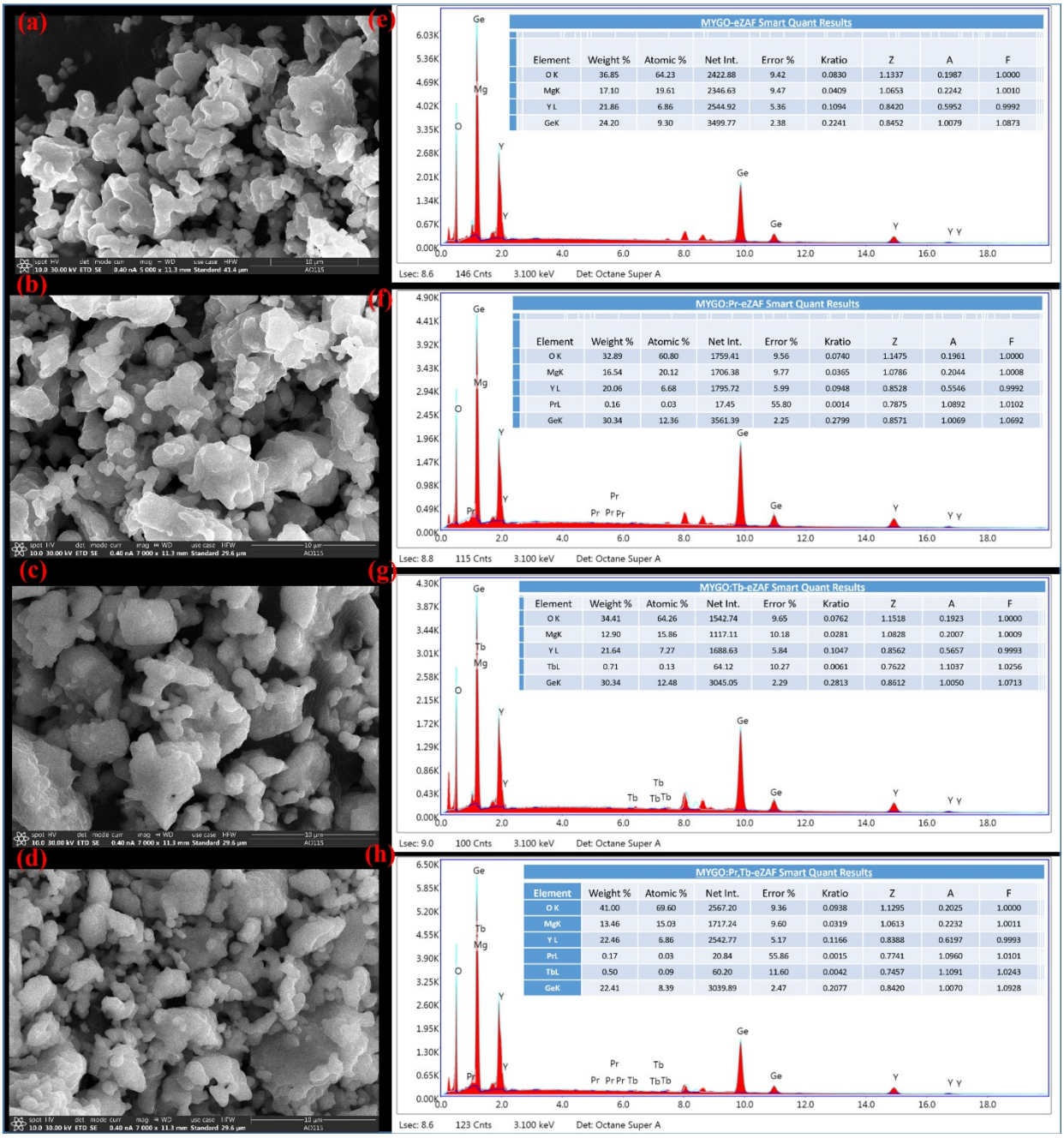

Fig. S3 (a-d) The SEM images of the phosphors of MYGO host (a), MYGO:Pr (b), MYGO:Tb (c) and MYGO:Pr,Tb (d). (e-h) The EDS of the phosphors of MYGO host (e), MYGO:Pr (f), MYGO:Tb (g) and MYGO:Pr,Tb (h).

Model	Gauss				
Equation	$y = y_0 + \{A/[w*sqrt(pi/2)]\} * exp(-2*[(x-x_c)/w) ^2]$				
Plot (PLE of Ce^{3+})	Peak 1	Peak 2	Peak 3	Peak 4	Peak 5
y_0/E-4	22.60 ± 0.68				
x_c	300.63 ± 2.93	319.00 ± 0.21	335.98 ± 1.28	426.30 ± 2.23	458.50 ±
w	51.67 ± 3.09	20.86 ± 0.72	22.38 ± 3.83	32.36 ± 0.39	48.42 ±
A	0.41 ± 0.12	2.72 ± 0.26	0.31 ± 0.12	12.04 ± 0.67	56.21 ±
Reduced Chi-Sqr	7.79E-6				
R^2 (COD)	0.9892				
Adj.R^2	0.9891				

Table S3 Parameter values about cumulative gauss fit curves for the PLE (λem = 537 nm) spectrum of MYGO:Ce.

n	Ln	ΔE (n+1, 7, 2+)	E_{fd} (n+1, 2+, free)	ΔE (n, 6, 3+)	E_{fd} (n, 3+, free)	E_{exch} (n, 3+, F)
0	La	5.61	-0.94	-	-	-
1	Ce	4.13	-0.35	5.24	6.12	-
2	Pr	2.87	1.56	3.39	7.63	-
3	Nd	2.43	1.93	1.9	8.92	-
4	Pm	2.34	1.96	1.46	9.24	-
5	Sm	1.25	3	1.27	9.34	-
6	Eu	0	4.22	0	10.5	-
7	Gd	4.56	-0.2	-1.34	11.8	-
8	Tb	3.31	1.19	3.57	7.78	1.0
9	Dy	2.27	2.17	2.15	9.25	0.74
10	Ho	2.4	2.25	1.05	10.1	0.51
11	Er	2.58	2.12	1.12	9.86	0.35
12	Tm	1.72	2.95	1.28	9.75	0.28
13	Yb	0.433	4.22	0.236	10.89	0.22
14	Lu	-	-	-1.02	12.26	0.15

Table S4 Parameter values (in eV) that define the 4f and 5d binding energy curves for the divalent and trivalent lanthanides in compounds.

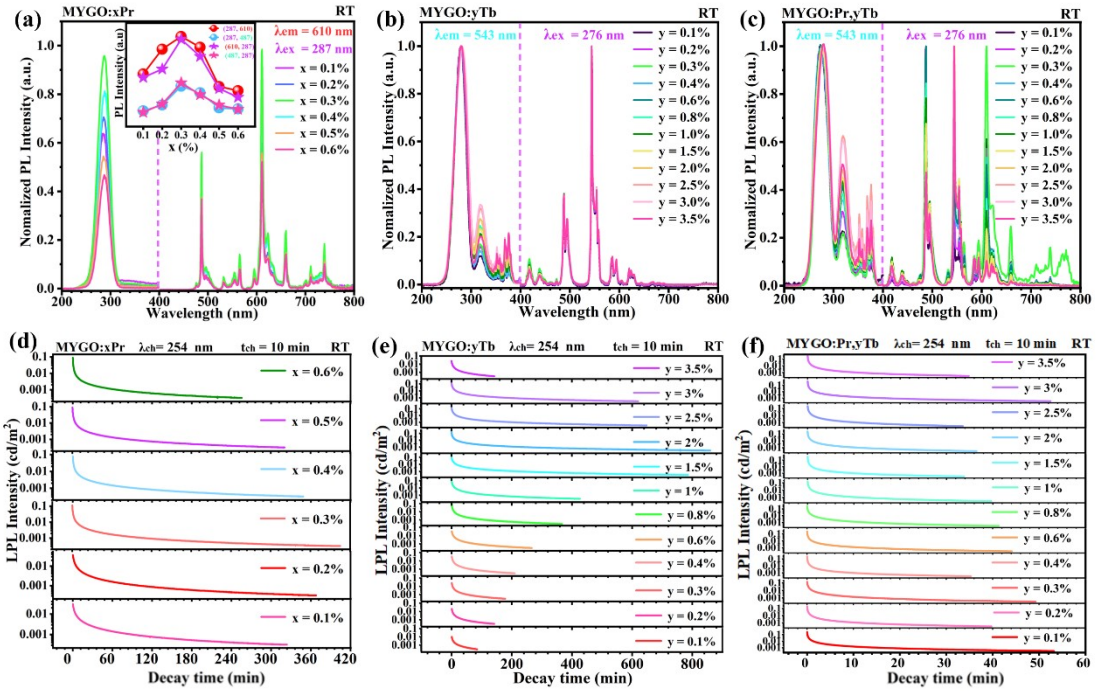

Fig. S4 (a-c) The PLE and PL spectra of the phosphors of MYGO:xPr (a), MYGO:yTb (b) and MYGO:Pr,yTb (c). (d-f) The LPL decay curves of the phosphors of MYGO:xPr (d), MYGO:yTb (e) and MYGO:Pr,yTb (f).

The PLE and PL spectra of the single-doped MYGO:xPr, and MYGO:yTb as well as co-doped MYGO:0.3%Pr,yTb (x:0.1%-0.6%, y:0.1%-3.5%) shown in **Fig. S4a-c**, measured at RT. In Fig. S4a, the intensity of Pr^{3+} characteristic peaks belonging to PLE (λ_{em} = 610 nm) and PL (λ_{ex} = 287 nm) spectra climbed to the strongest when x = 0.3%, and then decreased due to concentration quenching. The inset clearly shows this trend, what indicates that the optimal concentration of Pr^{3+} about fluorescence performance is x = 0.3%. Color-tuneability of Tb^{3+} doped phosphors have been observed in several oxide materials and is commonly associated with cross-relaxation and energy transfer processes.[3,4,8] Photoluminescence spectroscopy can be used to determine the dominant optical processes related to the tunable emission. RT PLE and PL spectra of MYGO samples containing 0.1–3.5% Tb^{3+} are shown in Fig. S4b. Two broad excitation peaks at ≈276 nm and 320 nm as well as several relatively weak and narrow peaks in the 345-395 nm range could be detected in the PLE spectra monitoring the 544 nm emission. The most intense excitation peak with a maximum at 276 nm is associated with 4f-5d transitions of Tb^{3+} and very similar to that for Pr^{3+}, so we will assign it to Tb^{3+} → CB IVCT. The assignment of the second broad excitation peak with a maximum at 320 nm is ambiguous in the investigated host, it could be attributed to either f-d transitions of Tb^{3+} in a distorted environment or related to point defects in the material. Several narrow excitation peaks in the 345–395 nm range can be assigned to the spin-forbidden f-f transition of Tb^{3+}. As expected, the intensity of these bands is relatively low in comparison to f-d excitation. Multiple luminescence bands in the 400-800 nm range associated with $^5D_3$ → ^7F_J and $^5D_4$ → ^7F_J transitions could be detected in the PL spectra shown in Fig. 3(b). The most intensive bands correspond to $^5D_3$ → $^7F_5$ (417 nm), $^5D_3$ → $^7F_4$ (438 nm), $^5D_4$ → $^7F_6$ (488 nm), $^5D_4$ → $^7F_5$ (544 nm), $^5D_4$ → $^7F_4$ (584 nm) and $^5D_4$ → $^7F_3$ (619 nm) transitions. And the relative intensity of $^5D_3$ → ^7F_J transitions decreases with the increase of Tb^{3+} content，which results in the changes in the emission color (see **Fig.3(c)**). Fig. S4c was analyzed in comparison with Fig. S4a-b, respectively, and the results shows that Due to the partial overlap of the excitation bands, the PL spectrum of co-doped MYGO:0.3%Pr,yTb has both Pr and Tb characteristic emission peaks under the characteristic Tb^{3+} excitation，which indicates that co-doping of Pr^{3+},Tb^{3+} in the host MYGO does not lead to the fluorescence completely quenching, and it is possible to realize the dual-luminescence centers, which is conducive to the realization of color-tunable multimode anti-counterfeiting applications.

To characterize LPL processes, The LPL decay curves have been analyzed. After pre-irradiated by 254 nm UV lamp

for 10 min at RT, all samples across varying Pr^{3+} and/or Tb^{3+} concentrations exhibited LPL phenomena as depicted in Fig. S4d-f. The phosphor exhibits bright initial LPL intensity. Subsequently, the LPL intensity is attenuated evidently at the first several minutes and then weakened slower and slower for a long time. Of these, Fig. 3(d) clearly shows this trend, with the initial LPL intensity increasing to a maximum over 100 mcd m^{-2} at x = 0.3% and then decreasing due to concentration quenching. And the doping sample MYGO:0.03%Pr showed the longest LPL lasting up to 405 min. The interplay between the LPL duration and Tb^{3+} concentration y is evident in Fig. 3(e), from which the better LPL properties are assigned to the 0.3% Tb^{3+}-doping MYGO sample. And analyzing the PL spectrum shown in Fig. 3(b), it is intuitive to find that MYGO:0.3%Tb has a strong emission peak in the short-wave region of 530-580 nm, which makes clear that the emission of MYGO:0.3%Tb has a larger energy difference with that of MYGO:Pr. These results indicate that co-doping Pr^{3+} with Tb^{3+} at a concentration of 0.3% is beneficial to achieve tunable multicolor luminescence for further precision anti-counterfeiting applications.

Fig. 3(f) shows the LPL decay curves of MYGO:0.3%Pr,yTb. MYGO:0.3%Pr,0.3%Tb exhibits excellent LPL performance although the decay trend is not in accordance with the traditional concentration quenching phenomenon. To explore the reasons for the unconventional decay trend of MYGO:0.3%Pr,yTb, analyzing the PL spectra, It is hypothesized that the LPL phenomenon also originates from the dual luminescence centers, Pr^{3+} and Tb^{3+}. The two luminescence centers interact with each other, resulting in the trend of the LPL decay curves that do not conform to a single ion concentration quenching phenomenon. Analyzed the Fig. 3(a-f), it have been determined that the x and y = 0.3% sample MYGO:Pr,Tb is the most suitable sample for subsequent characterization and application.

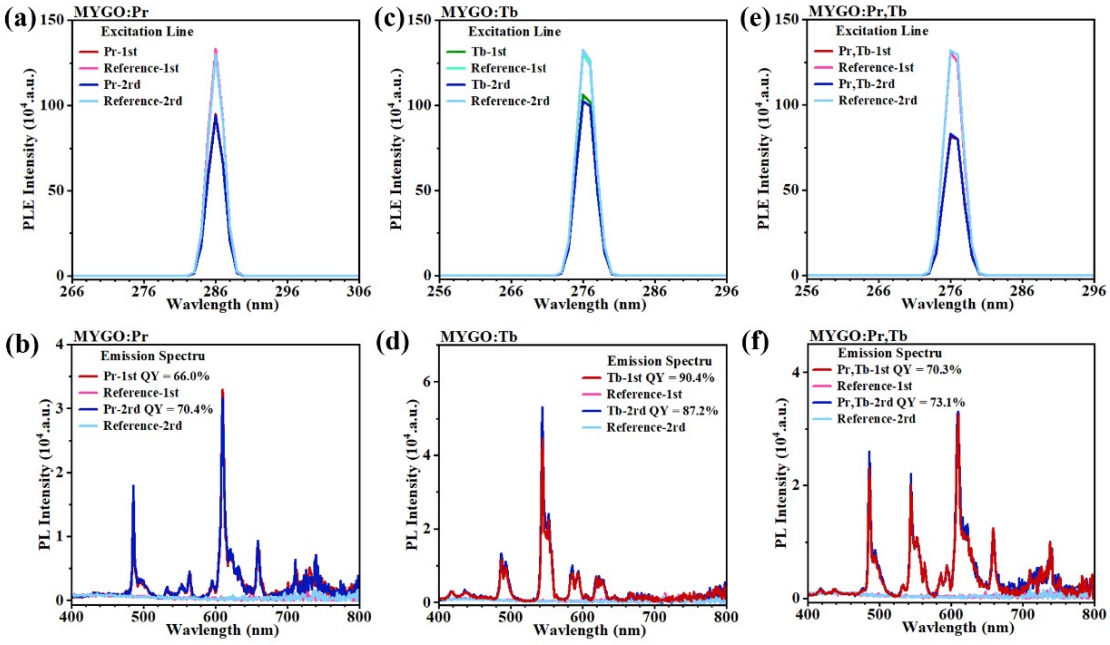

Fig. S5. PL spectra of MYGO:Pr (a,b) MYGO:Tb (c,d), MYGO:Pr,Tb (e,f), Each sample was repeated two times and the average PLQYs were calculated to 68.2%, 88.8%, 71.1%.

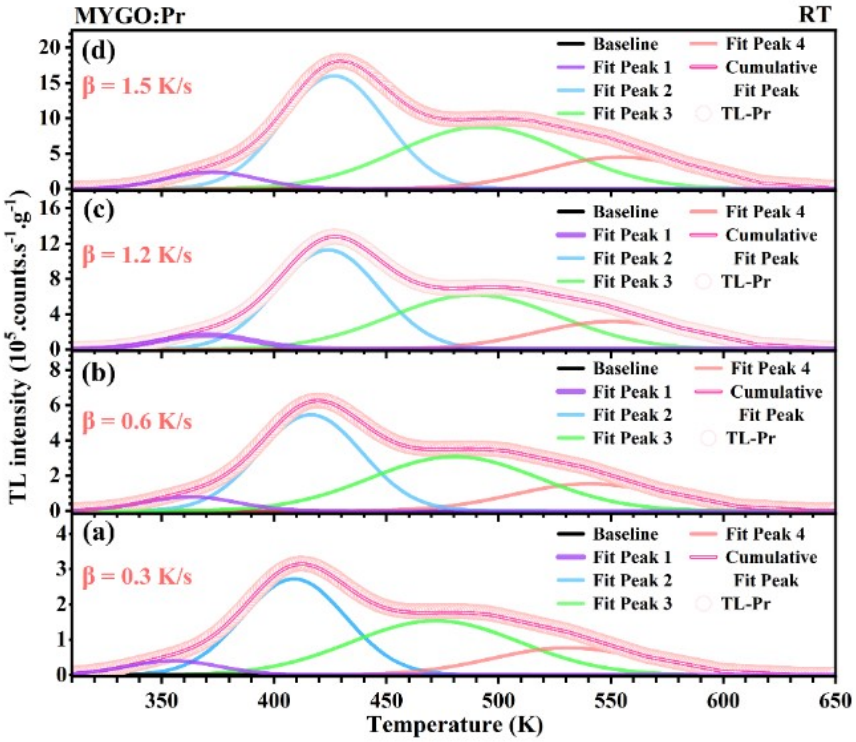

Fig. S6 The fitting TL curves of the bands H and P in MYGO:Pr. And the bands P decided by Pr^{3+} under some heating rates of 0.3 (a), 0.6 (b), 1.2 (c),1.5 (d) K s^{-1}, respectively.

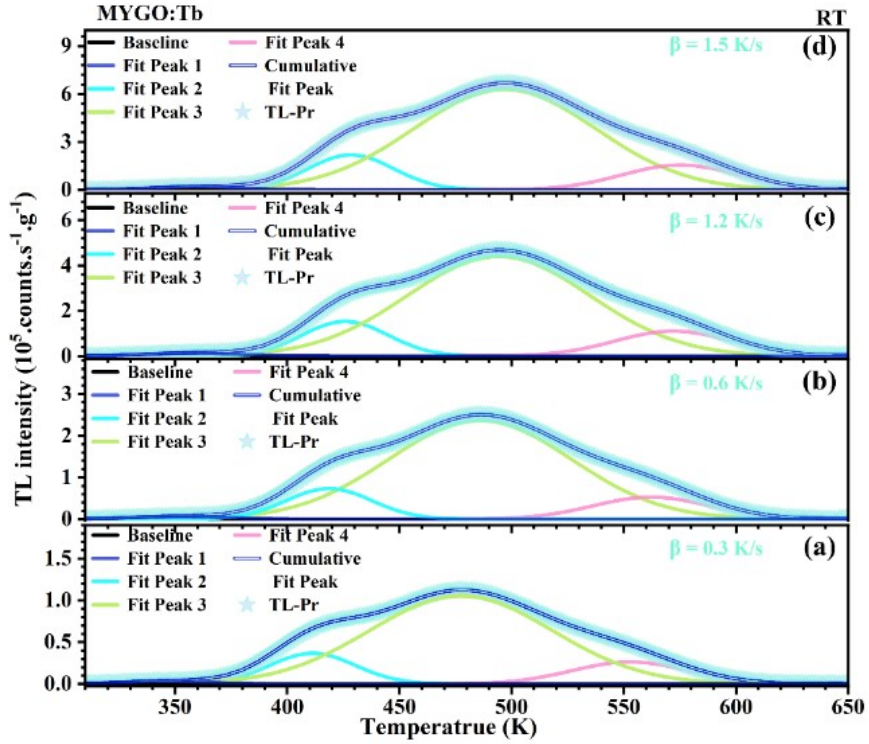

Fig. S7 The fitting TL curves of the bands H and T in MYGO:Tb. And the bands T decided by Tb^{3+} under some heating rates of 0.3 (a), 0.6 (b), 1.2 (c),1.5 (d) K s^{-1}, respectively.

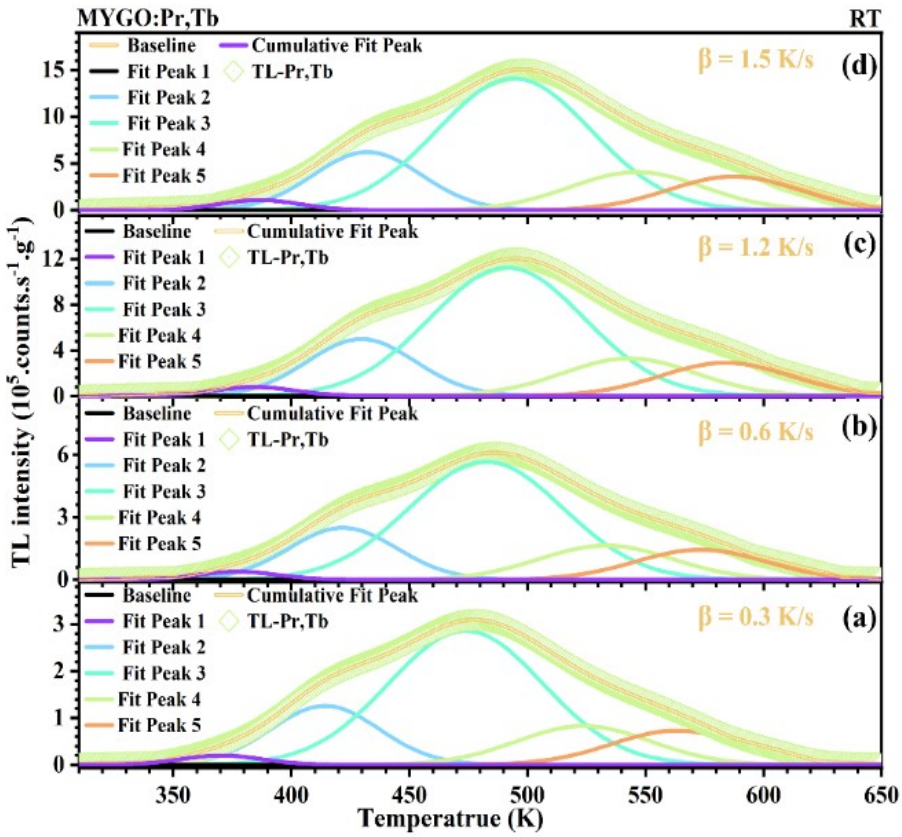

Fig. S8 The fitting TL curves of the bands H, P, and T in MYGO:Pr,Tb. And the bands P/T decided by Pr^{3+}/Tb^{3+} under some heating rates of 0.3 (a), 0.6 (b), 1.2 (c),1.5 (d) K s^{-1}, respectively.

Model	Gauss			
Equation	$y = y_0 + \{A/[w*sqrt(pi/2)]\} * exp(-2*[(x-x_c)/w) ^2]$			
Plot	Peak 1	Peak 2	Peak 3	Peak 4
y_0/E5	1.29 ± 0.04			
x_c	381.68 ± 1.11	422.10 ± 0.66	483.59 ± 2.32	546.04 ± 3.89
w	43.38 ± 1.12	34.38 ± 3.30	64.10 ± 2.92	87.73 ± 3.28
A/E7	2.91 ± 0.94	7.59 ± 1.12	10.10 ± 1.13	17.46 ± 1.57
Reduced Chi-Sqr	1.33E9			
R^2 (COD)	0.99854			
Adj.R^2	0.9985			

Table S5 Parameter values about cumulative gauss fit curves for the TL curve of MYGO:Pr at 1.0 K s^{-1}.

Model	Gauss			
Equation	$y = y_0 + \{A/[w*sqrt(pi/2)]\} * exp(-2*[(x-x_c)/w) ^2]$			
Plot	Peak 1	Peak 2	Peak 3	Peak 4
y_0/E4	1.56 ± 0.63			
x_c	353.04 ± 0.94	423.65 ± 0.13	491.63 ± 0.17	569.84 ± 0.49
w	33.54 ± 1.98	37.41 ± 0.55	87.10 ± 0.99	50.17 ± 0.79
A/E7	2.91 ± 0.94	7.59 ± 1.12	10.10 ± 1.13	17.46 ± 1.57
Reduced Chi-Sqr	6.80E8			
R^2 (COD)	0.9915			
Adj.R^2	0.9914			

Table S6 Parameter values about cumulative gauss fit curves for the TL curve of MYGO:Tb at 1.0 K s^{-1}.

Model	Gauss				
Equation	$y = y_0 + \{A/[w*sqrt(pi/2)]\} * exp(-2*[(x-x_c)/w) ^2]$				
Plot	Peak 1	Peak 2	Peak 3	Peak 4	Peak 5
y_0/E4	4.00 ± 0.11				
x_c	379.86 ± 5.23	427.69 ± 0.51	486.29 ± 1.47	540.45 ± 3.05	582.05 ± 2.33
w	76.89 ± 3.43	31.77 ± 1.43	67.72 ± 2.84	38.90 1.85	60.99 ± 8.06
A/E7	58.91 ± 9.10	8.58 ± 1.39	141.97 ± 11.04	4.63 ± 0.05	45.41 ± 3.72
Reduced Chi-Sqr	2.24E9				
R^2 (COD)	0.9930				
Adj.R^2	0.9930				

Table S7 Parameter values about cumulative gauss fit curves for the TL curve of MYGO:Pr,Tb at 1.0 K s^{-1}.

T (K) \ *β* (K/s)		0.3	0.6	1.0	1.2	1.5
MYGO:Pr	Fit Peak 1	369.1	376.7	382.5	383.9	386.3
	Fit Peak 2	408.8	416.2	422.0	424.0	426.6
	Fit Peak 3	471.9	480.4	487.1	489.4	492.4
	Fit Peak 4	531.9	541.6	549.0	551.7	555.0
MYGO:Tb	Fit Peak 1	343.4	439.6	354.1	355.6	357.5
	Fit Peak 2	410.3	417.6	422.8	424.8	427.3
	Fit Peak 3	477.4	485.9	491.5	494.2	496.9
	Fit Peak 5	552.4	561.8	569.0	571.6	574.8
MYGO:Pr,Tb	Fit Peak 1	370.4	377.2	382.3	384.2	386.5
	Fit Peak 2	414.2	421.8	427.5	429.6	432.2
	Fit Peak 3	473.9	482.5	489.0	491.4	494.3
	Fit Peak 4	523.8	533.3	540.5	543.1	546.4
	Fit Peak 5	563.2	573.4	581.0	584.0	587.5

Table S8 The Tm values of the bands H (Fit Peak 1-3), the bands P (Fit Peak 4) or/and the bands T (Fit Peak 5) in MYGO:Pr or/and Tb under some heating rates of 0.3 (a), 0.6 (b), 1.2 (c),1.5 (d) K s^{-1}, respectively.

E (eV) \ *s* (s^{-1})		Trap1	Trap2	Trap3	Trap4	Trap5
MYGO:Pr	*E*	1.160	1.285	1.489	1.684	-
	s	1.861E14	1.557E14	1.892E14	2.763E14	-
	R^2	0.9920	0.9866	0.9849	0.9943	
MYGO:Tb	*E*	1.147	1.377	1.6088	-	1.867
	s	2.301E15	1.853E15	1.561E15	-	9.2071E14
	R^2	0.9942	0.9878	0.9964		0.9801
MYGO:Pr,Tb	*E*	1.168	1.310	1.504	1.667	1.796
	s	2.70E14	1.062E14	1.757E14	3.679E14	5.153E14
	R^2	0.9921	0.9992	0.9972	0.9792	0.9967

Table S9 The Trap depth and s values of the bands H (Fit Peak 1-3), the bands P (Fit Peak 4) or/and the bands T (Fit Peak 5) in MYGO:Pr or/and Tb

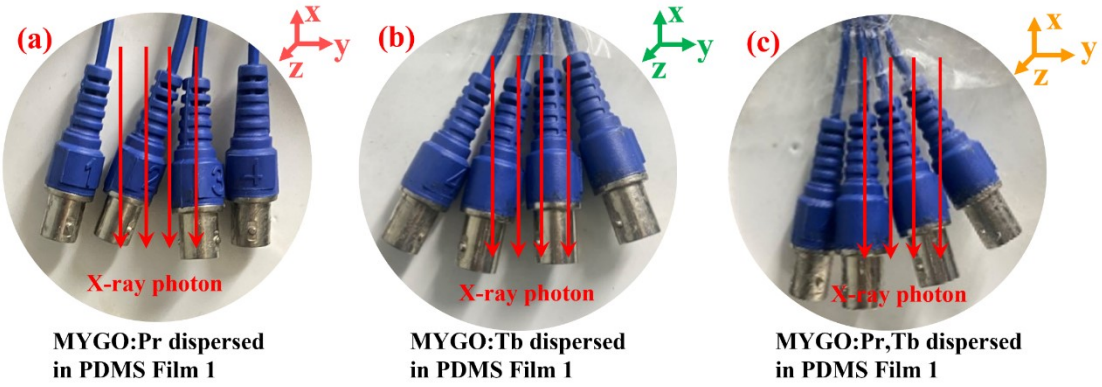

Fig. S9 the films placed under the four large wire connectors. Charging by X ray.

References

1. Z. Fan, S. Bi and H. J. Seo, Tunable emission via dual-site occupancy in $Ba_2CaB_2Si_4O_{14}$: Bi^{3+}, Sm^{3+} phosphors, *Journal of Alloys and Compounds*, 2022, **916**.
2. F. Xie, J. Li, D. Xu, et al., Layer-structure-suppressed concentration quenching of Dy^{3+} luminescence and the realization of a single phase white light-emitting phosphor cooperated with Tm^{3+}, *Inorganic Chemistry Frontiers*, 2022, **9**, 3797-3807.
3 A. Mao, Z. Zhao, J. Wang, et al., Crystal structure and photo-luminescence of $Gd_3Ga_2(Al_{3-x}Si_x)(O_{12-x}N_x)$:$Ce^{3+}$ phosphors for AC-warm LEDS, *Chemical Engineering Journal*, 2019, **368**, 924-932.
4. Y. Lin, C. Ming, Z. Wang, et al., Co-doped long persistent luminescence materials $LiSr_3SiO_4Cl_3$:Eu^{2+},Ln^{3+} (Ln = Dy, Ho, Er): construction and verification of VRBE and HRBE scheme and their multifunctional applications, *Inorganic Chemistry Frontiers*, 2023, **10**, 5071-5081.
5. P. Dorenbos, Ce^{3+} 5d-centroid shift and vacuum referred 4f-electron binding energies of all lanthanide impurities in 150 different compounds, Journal of Luminescence, 2013, **135**, 93-104.
6. H. Lin, B. Wang, J. Xu, et al., Phosphor-in-Glass for High-Powered Remote-Type White AC-LED, *ACS Applied Materials & Interfaces*, 2014, **6**, 21264-21269.
7. S. Ding, P. Chen, H. Guo, et al., Crystal structure and optical performance analysis of a new type of persistent luminescence material with multi-functional application prospects, *Journal of Energy Chemistry*, 2022, **69**, 150-160.